

Enhancing High Voltage Stability via Fluorination of Functionalized Metal Organic Framework Electrolyte in Lithium Metal Batteries

Chenxi Xiao^{+, [a, b]} Xiaotong Liu^{+, [a]} Weiping Li^{, [a, b]} Xianghe Ma,^[a] Ju Qian,^[a, b] and Xinrong Lin^{*[a, b]}

The electrolyte stability under high-voltage conditions considerably limits the upper cut-off potential of solid-state electrolytes (SSEs) and therefore the energy density of all-solid-state batteries (ASSBs). In this work, metal-organic frameworks (MOFs) were fluorinated to lower the energy level of HOMO orbital and allow access to a 4F-MOF that exhibit enhanced anodic stability. The composited 4F-MOF/PEO electrolyte could not only transport Li^+ ions in the ordered framework channels, but also provide a remarkable high-voltage stability up to 5.0 V, shielding oxidative decomposition that would otherwise occur

at around 3.9 V for conventional PEO electrolytes. In addition, stable lithium deposition was demonstrated for more than 1,300 hours at $0.1 \text{ mA}\cdot\text{cm}^{-2}$, while reversible charge-discharge cycling performance was delivered in assembled $\text{Li}||\text{LiNi}_{0.5}\text{Mn}_{1.5}\text{O}_4$ (LNMO) ASSBs up to 5.0 V. Post-mortem X-ray photoelectron spectroscopy (XPS) investigation on cathodes revealed presence of a LiF-rich cathode electrolyte interface (CEI), supporting promoted stability towards high-voltage ASSBs.

Introduction

As electric vehicles and grid-scale applications continue to proliferate rapidly, the imperative lies in the development of rechargeable batteries with high energy densities.^[1] Li metal batteries (LMBs) have garnered increasing attention due to their low electrode potential (-3.04 V) and high theoretical specific capacity ($3860 \text{ mAh}\cdot\text{g}^{-1}$) associated with Li metal anodes.^[2-3] In essence, a high-performance LMB should exhibit attributes such as a high working voltage, stable electrolyte-electrode interphase, reversible capacity and long cycle life.^[2,4] However, conventional electrolyte materials, be it liquid solvents, polymers, ceramics or their composites, are thermodynamically limited and can react with lithium metal or the cathodes, leading to the formation of a solid electrolyte interphase (SEI) and unstable cathode-electrolyte interphase (CEI).^[5-6] Such instability leads to continuous electrolyte consumption, formation of inactive Li, and parasitic reactions/dissolution of cathodes.

Solid-state electrolytes (SSEs) represent a promising class of materials in battery technologies to access all-solid-state

batteries (ASSBs).^[7-8] These innovations address critical challenges associated with traditional liquid electrolytes and offer a safer alternative to their liquid counterparts.^[9-12] In the meantime, porous coordination polymers, such as metal-organic frameworks (MOFs) have garnered increasing attention as SSEs due to their unique characteristics originated from their porous nature, which gives rise to well-defined ion-conducting pathways within their intricate crystalline structures.^[13-15] These pathways serve as channels through which lithium ions can move freely, facilitating efficient ion transport. This controlled ionic mobility not only enhances the overall ionic conductivity of the electrolyte but also helps prevent the formation of dendrites.^[16] More importantly, the stability of MOFs is a crucial advantage in their application as solid electrolytes, which exhibit remarkable thermal and chemical stability, ensuring their integrity under the demanding conditions.^[17]

Beyond MOF-based electrolytes, the energy density of a battery system is inherently constrained by the voltage window in addition to specific capacity of the cathode materials, which is determined by the energy gaps between the highest occupied molecular orbital (HOMO) and the lowest unoccupied molecular orbital (LUMO) of the electrolyte materials.^[6,18] Prior investigations have revealed that fluorination in molecules could enlarge energy gap between HOMO and LUMO, in addition to affording favorable characteristics such as superior thermal and chemical stability, as well as weakly solvation effect.^[19-23] In particular, these molecules showed enhanced oxidation stability at elevated cut-off voltages above 4.4 V (vs. Li/Li^+).^[24-25] This stands in contrast to conventional nonfluorinated solvents or polymers with compromised oxidative stability. For examples, the commonly used polyethylene oxide (PEO) exhibits substantial decomposition beyond 3.9 V,^[26] failing

[a] C. Xiao,⁺ X. Liu,⁺ W. Li, X. Ma, J. Qian, Prof. X. Lin

School of Chemical Science and Technology

Yunnan University

Kunming 650091, China

E-mail: xrlin@ynu.edu.cn

[b] C. Xiao,⁺ W. Li, J. Qian, Prof. X. Lin

Division of Natural and Applied Sciences

Duke Kunshan University

Jiangsu 215306, China

[†] These authors contributed equally to this work.

 Supporting information for this article is available on the WWW under <https://doi.org/10.1002/batt.202400078>

to couple with high-voltage positive electrodes such as $\text{LiNi}_{0.5}\text{Mn}_{1.5}\text{O}_4$ (LNMO).^[27]

We envisioned that fluorinated MOF could provide an oxidation-free and porous backbone that allows working cut-off voltages extension of PEO-based composite electrolytes. In this study, we tuned the HOMO energy level via synthesizing a fluorinated metal-organic framework (4F-MOF). Density functional theory (DFT) calculation revealed increasingly reduction of HOMO orbital levels with increasing degree of fluorination. Further compositing the 4F-MOF with PEO, on the one hand could potentially provide ordered channels for more stable lithium deposition; On the other hand, the parasitic oxidation reactions of PEO were effectively shielded through the addition of 4F-MOF. As a result, an SSE containing 50 wt% of 4F-MOF exhibited good lithium deposition stability and cycled for more than 1,300 hours at $0.1 \text{ mA} \cdot \text{cm}^{-2}$, demonstrating no sign of dendritic lithium electrodeposition. Furthermore, ASSBs were assembled and cycled in high voltage cathodes with 5-V cathode LNMO, representing a significant improvement in comparison to conventional PEO-based ASSBs. The unique attributes of 4F-MOF, including its role as a fluorinated electrolyte, its porous structure, and its influence on interfacial stability, collectively resulted in substantial advancements in the stability and cyclability of lithium batteries, presenting a promising avenue for the development of next-generation energy storage technologies.

Results and Discussion

To prepare the fluorinated MOF, we used tetrafluoroterephthalic acid (TFBDC) as a ligand to introduce C–F bond in MOF and achieve fluorine functionalization (Figure 1a). We selected Zr-based UIO-66 backbone as the matrix MOF material for their good thermal and chemical innerness.^[28] TFBDC was reacted with equivalent stoichiometric ratio of ZrCl_4 in an acetic acid/water solution to yield 4F-MOF. As shown in Figure 1b, 4F-MOF comprises of tetrafluoroterephthalic acid as the bridging organic ligands, with Zr as the metal center. The as-synthesized 4F-MOF was characterized by X-ray diffraction (XRD). As revealed in Figure 1c, the experimental curve was slightly different from the simulation results, presumably caused by possible presence of ligand defects and agreed well with previous reports.^[29] We carried out Brunauer-Emmett-Teller analysis to examine the pore structures and surface areas of the functionalized MOF by measuring nitrogen adsorption and desorption isotherms. As shown in Figure 1d, the result revealed that the pore aperture of 4F-MOF measured at 19 \AA . This measurement aligned with the typical characteristics of MOF structures, which could offer an advantage by providing additional channels for the transport of Li^+ with a radius of approximately 0.76 \AA . In contrast to the freely shuffling Li^+ ions, the movement of bulky counter-anions, such as TFSI^- would be retarded, reducing the concentration polarization in the process of charge and discharge. Additionally, thermogravimetric analysis (TGA) of 4F-MOF was investigated to probe the thermal stability (Figure S2). After normalizing the weight loss before

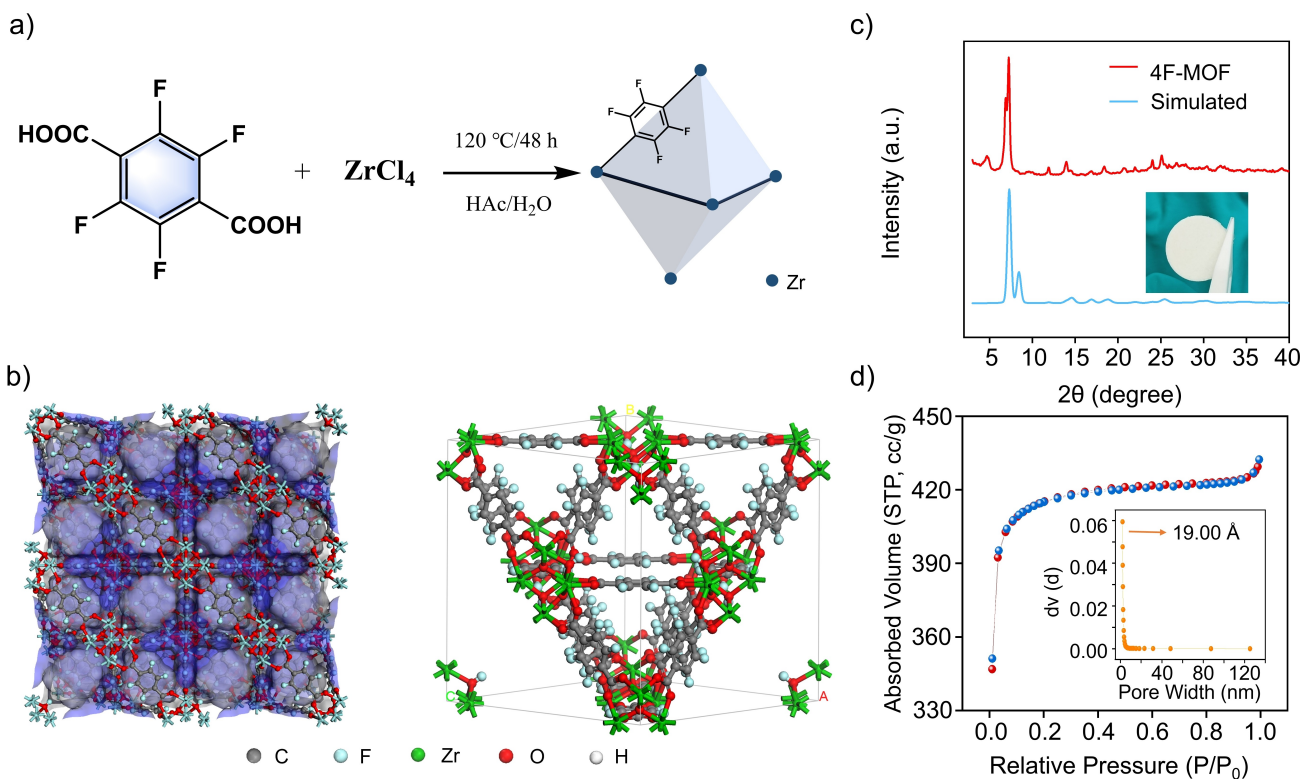


Figure 1. (a) Schematic of synthesized 4F-MOF. (b) 3D structure simulation diagram of 4F-MOF. (c) XRD spectra of 4F-MOF. (d) Adsorption-desorption curves of 4F-MOF via Brunauer-Emmett-Teller analysis.

100 °C as a result of inevitable H₂O and solvents originated from the activation process, thermal decomposition of 4F-MOF was observed to start at around 350 °C (10% weight loss), agreeing with typical MOF materials that exhibit excellent thermal stability.

Density functional theory (DFT) simulations were performed to investigate thermodynamic stability of the ligand units constituting 4F-MOF. Figure 2a exhibits the chemical structure of the bridging organic ligands, which were varied from fluorinated ligands of tetrafluoroterephthalic acid and 2,6-fluoroterephthalic acid, to terephthalic acid. The comparison shows that fluorination lowered the HOMO orbital and expanded the HOMO-LUMO energy gap, which is beneficial for the enhancement of the oxidative stability of MOF structure in solid-state electrolytes. Therefore, 4F-terephthalic acid was chosen to serve as the chelating ligand and was denoted as 4F-MOF in the following studies. PEO was composited to provide ion transport matrix and better coordination with Li⁺ ions, while a -3.61 eV of adsorption energy was found between PEO and 4F-MOF via DFT simulation, presumably due to coordination between metal and ether linkages of PEO. Lithium bis(trifluoromethanesulphonyl)imide (LiTFSI) in the molar ratio of 1:18 was added into the SSE to provide Li⁺ ion source.

In order to experimentally explore the influence of 4F-MOF on the stability of electrolyte, we varied the doping amount of 4F-MOF and characterized electrochemical stability in Li||stainless steel (SS) cells via linear sweep voltammetry (LSV, Figure 2c), where the first cathodic and anodic scans are shown. We defined 0.05 mA of current increase as the cut-off voltage of electrolyte decomposition, and observed that the overall stability window expanded as the amount of 4F-MOF increased. The cathodic curves overlapped with each other between 0–0.5 V without notably distinct trend of stability, which corresponds to typical Li deposition peaks. The peak at around 1.0 V was attributed to the decomposition of LiTFSI. On the other hand, the onset of oxidation was postponed notably as a function of the degree of fluorination. Closer examination of Figure 2d showed that 50% 4F-MOF/PEO didn't start to oxidize until 5.1 V. As a control group, PEO was oxidized at 3.9 V, showing limited compatibility with high-voltage electrodes. To better gauge the stability of 50% 4F-MOF/PEO at high cut-off voltages in longer duration, we performed electrochemical floating test from 4.2 to 5.0 V. As shown in Figure 2e, it is evident that simple PEO underwent oxidative degradation beyond the tested voltage at 3.9 V, while the incorporation of 50% 4F-MOF sustained an anodic voltage extension up to 5 V, demonstrating the remarkable oxidative stability and potential application of

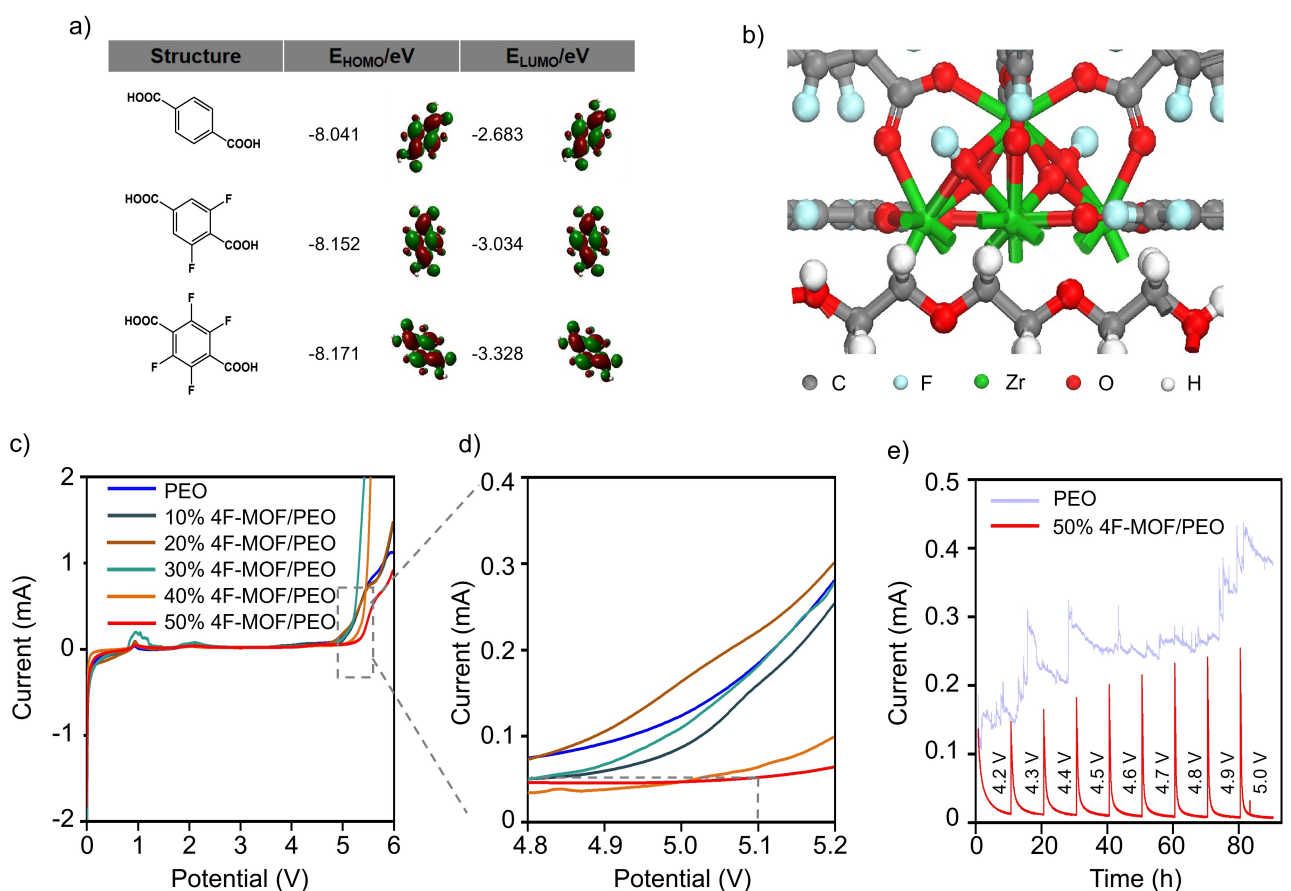


Figure 2. (a) Calculations of HOMO and LUMO energy levels via DFT based on different bridging organic ligands. (b) Adsorption between 4F-MOF and PEO composite solid-state electrolyte. (c) LSV curves of solid-state electrolytes based on different amounts of 4F-MOF in PEO-composite electrolyte. (d) Enlarged oxidation voltages of different solid-state electrolytes. (e) Electrochemical floating test for 50% 4F-MOF/PEO and PEO varying from 4.2 to 5.0 V.

4F-MOF in the regime of high 4-V electrodes and 5-V electrodes. In addition, to illustrate that fluorination benefits the oxidation stability of MOF, we prepared 50% MOF/PEO without any fluorination on the MOF to compare with 50% 4F-MOF/PEO. As shown in Figure S3, while 50% MOF/PEO showed inferior oxidative stability until 4.2 V, 50% 4F-MOF/PEO showed much higher anodic voltage at 5.1 V.

Next, we carried out electrochemical impedance spectroscopy (EIS) to measure the bulk resistance of the 4F-MOF/PEO electrolytes at 60°C. We first compared the ionic conductivity between 50% MOF/PEO and 50% 4F-MOF/PEO. As shown in Figure S4, 50% 4F-MOF/PEO ($1.85 \times 10^{-4} \text{ S} \cdot \text{cm}^{-1}$) exhibited a higher ionic conductivity than the 50% MOF/PEO ($1.58 \times 10^{-4} \text{ S} \cdot \text{cm}^{-1}$) due to fluorination, indicating that fluorination can accelerate the migration of Li^+ in pores of MOF.^[30] As shown in Figure 3a, increasing weight percentage of 4F-MOF in PEO from 10 to 50 wt% increased the impedance of the resultant solid-state electrolytes, presumably owing to accumulation of excess 4F-MOF particles that blocked the migration channel of Li^+ . Despite of that, we focused on 50% 4F-MOF/PEO for the consideration of higher voltage tolerance given sufficient ionic conductivity of 50% 4F-MOF/PEO at 60°C, which was characterized as a function of temperature and measured to be $1.85 \times 10^{-4} \text{ S} \cdot \text{cm}^{-1}$ at 60°C (Figure 3b). Fitting the temperature curve with Vogel-Tamman-Fulcher (VTF) equation resulted in an activation energy of 0.32 eV. The exchange current density (j_0) was calculated to further investigate Li^+ transfer kinetics at the interface (Figure 3c) by fitting with the Tafel plot of various electrolytes. The smaller Tafel slope of 50% 4F-MOF/PEO indicated slower faradic reaction kinetics at the electrolyte-electrode interface, which was ascribed to slower Li^+ transport contributed by high concentration of 4F-MOF and agreed well with ionic conductivity measurements. The lithium ion transference number (t_{Li^+}) of 50% 4F-MOF/PEO was measured to be 0.39, which is higher than pure PEO at 0.19, benefitted from the weakly solvating effect of fluorine-containing substituents (Figure 3d).

PEO indicated slower faradic reaction kinetics at the electrolyte-electrode interface, which was ascribed to slower Li^+ transport contributed by high concentration of 4F-MOF and agreed well with ionic conductivity measurements. The lithium ion transference number (t_{Li^+}) of 50% 4F-MOF/PEO was measured to be 0.39, which is higher than pure PEO at 0.19, benefitted from the weakly solvating effect of fluorine-containing substituents (Figure 3d).

The Li stripping/plating performance in $\text{Li}||\text{Li}$ symmetrical cells of 50% 4F-MOF/PEO was investigated with a current capacity of $0.1 \text{ mA} \cdot \text{cm}^{-2}$ in comparison with the PEO control group. As shown in Figure 4a, the symmetrical cell assembled with 50% 4F-MOF/PEO displayed a remarkably extended cycling life, surpassing 1,300 hours under the tested conditions. In contrast, even though PEO afforded relatively small overpotential of 12 mV because of its greater Li^+ transport ability, it delivered a short cycling length of 170 h and rapidly decayed afterwards, indicating cell short-circuit. When the current density was increased to $0.2 \text{ mA} \cdot \text{cm}^{-2}$, as shown in Figure 4b, the symmetrical cell with 50% 4F-MOF/PEO showed a stable cycling over 500 h, whereas the cell with PEO quickly short-circuited within 90 hours. Given the unique properties of 4F-MOF and the Li–F interactions that were revealed previously, the excellent performance of lithium stripping/plating was attributed to more uniform Li^+ distribution and transport in the ordered and microporous structure of 4F-MOF, allowing for homogenous ion transport in between the electrodes. To examine the morphological changes at the interface that resulted in the significantly different Li deposition behavior, the

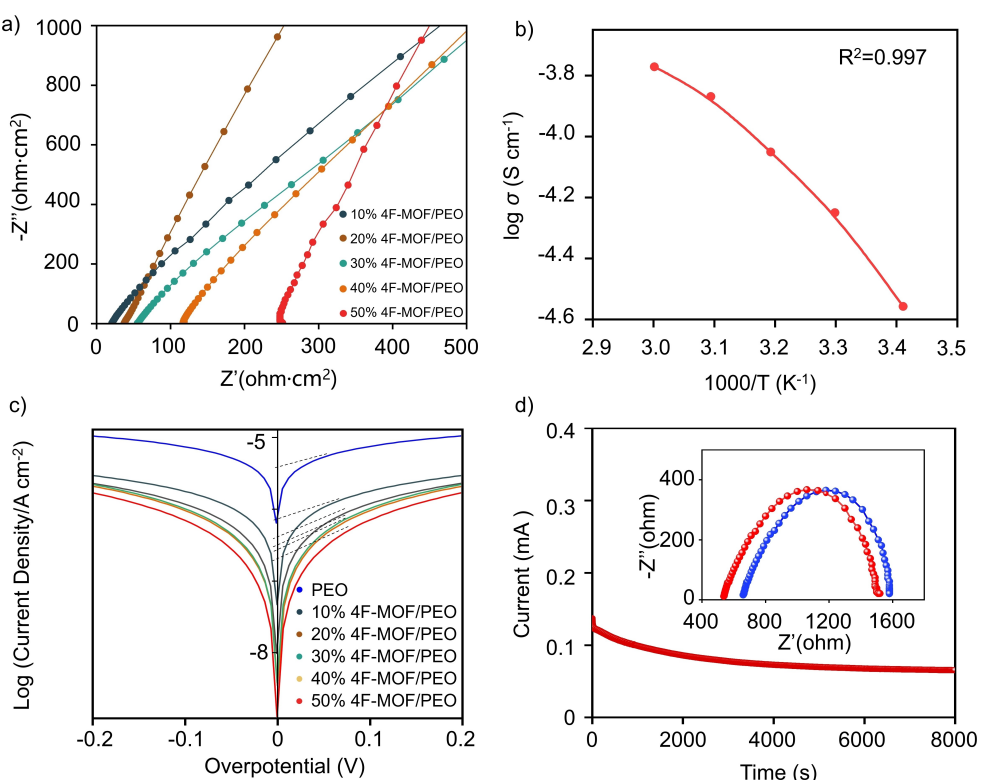


Figure 3. (a) Impedance measurements via EIS with varying amount of 4F-MOF/PEO at 60 °C. (b) Ionic conductivity of 50% 4F-MOF/PEO from 20–60 °C. (c) Tafel plot of different solid-state electrolytes with varying amount of 4F-MOF. (d) Measurement of Li^+ transference number of 50% 4F-MOF/PEO electrolyte.

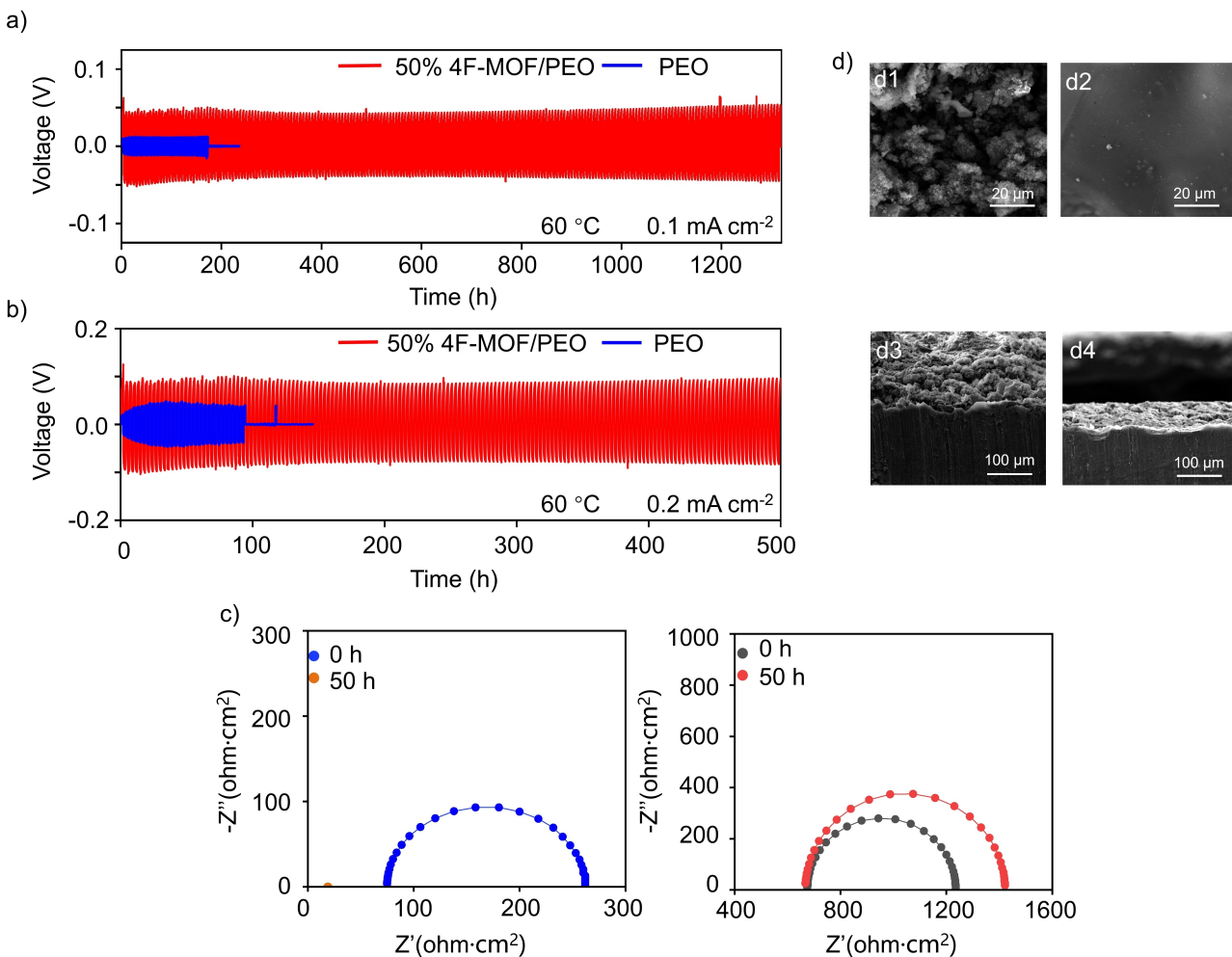


Figure 4. (a) Long-term cycling investigations of $\text{Li} \parallel \text{Li}$ symmetric cells with 50 % 4F-MOF/PEO and PEO at 60°C under current density of $0.1 \text{ mA}\cdot\text{cm}^{-2}$. (b) Long-term cycling investigations of $\text{Li} \parallel \text{Li}$ symmetric cells with 50 % 4F-MOF/PEO and PEO at 60°C under current density of $0.2 \text{ mA}\cdot\text{cm}^{-2}$. (c) EIS of PEO and 50 % 4F-MOF/PEO after cycling investigations. (left) PEO, (right) 50 % 4F-MOF/PEO. (d) SEM images of lithium dendrite growth at the electrode-electrolyte interface after 50 h.

comparison of the lithium anode surface after 100 h of cycling between 50 % 4F-MOF/PEO and pure PEO was performed by post-mortem scanning electron microscopy (SEM, Figure 4d). It is evident that dendrite nucleation was alleviated on the plating lithium anode for 50 % 4F-MOF/PEO, while heterogenous nucleation was clearly observed for PEO electrolytes during the same time period. Furthermore, impedance of the cells at different time slots was monitored by EIS cycling at the current density of $0.2 \text{ mA}\cdot\text{cm}^{-2}$. As shown in Figure 4c, the overall resistance of PEO declined to almost zero after 50 hours, suggesting cell short-circuit resulted from dendritic lithium penetration. On contrary, the bulk resistance of the 50 % 4F-MOF/PEO electrolyte slightly changed from 674.4 to $667.3 \Omega\cdot\text{cm}^2$, while interfacial resistance increased from 561.1 to $754.0 \Omega\cdot\text{cm}^2$, attributed to the formation of an effective SEI and passivation at the electrode-electrolyte interface.

Finally, galvanostatic charge-discharge cycling was performed to demonstrate the practical applicability of 50 % 4F-MOF/PEO in high-voltage ASSBs by assembling full cells. Lithium anode was firstly combined with LNMO and charged to

4.6 V (Figure 5a). The cell had an initial specific capacity of $93.5 \text{ mAh}\cdot\text{g}^{-1}$ at a C-rate of 0.1 C at 60°C . The coulombic efficiency quickly reached and stabilized at around 99 % in the initial cycles. Upon cycling, the cell showed 96 % capacity retention after 150 cycles. As a comparison, PEO-containing cells are not compatible with such high voltage and failed to even start cycling in this experiment. Further, as shown in Figure 5b, it can be seen that when charged to 4.7 V, 50 % 4F-MOF/PEO-contained cells were still sustainable, affording a specific capacity at $83.0 \text{ mAh}\cdot\text{g}^{-1}$. In order to further prove the high voltage resistance of 50 % 4F-MOF/PEO electrolyte, LNMO cathodes combining with Li anode was assembled as ASSBs and upper cut-off voltage was extended up to 5 V. Notably, the 50 % 4F-MOF/PEO electrolyte containing strong C–F bonds and reduced HOMO energy levels enabled the charge-discharge cycling at 5.0 V and exhibited stable discharge capacities at around $80.0 \text{ mAh}\cdot\text{g}^{-1}$ (Figure 5c). As a comparison, when the cycle performance of 50 % MOF/PEO without fluorination was tested at 4.7 V (Figure S9), the capacity quickly decayed from

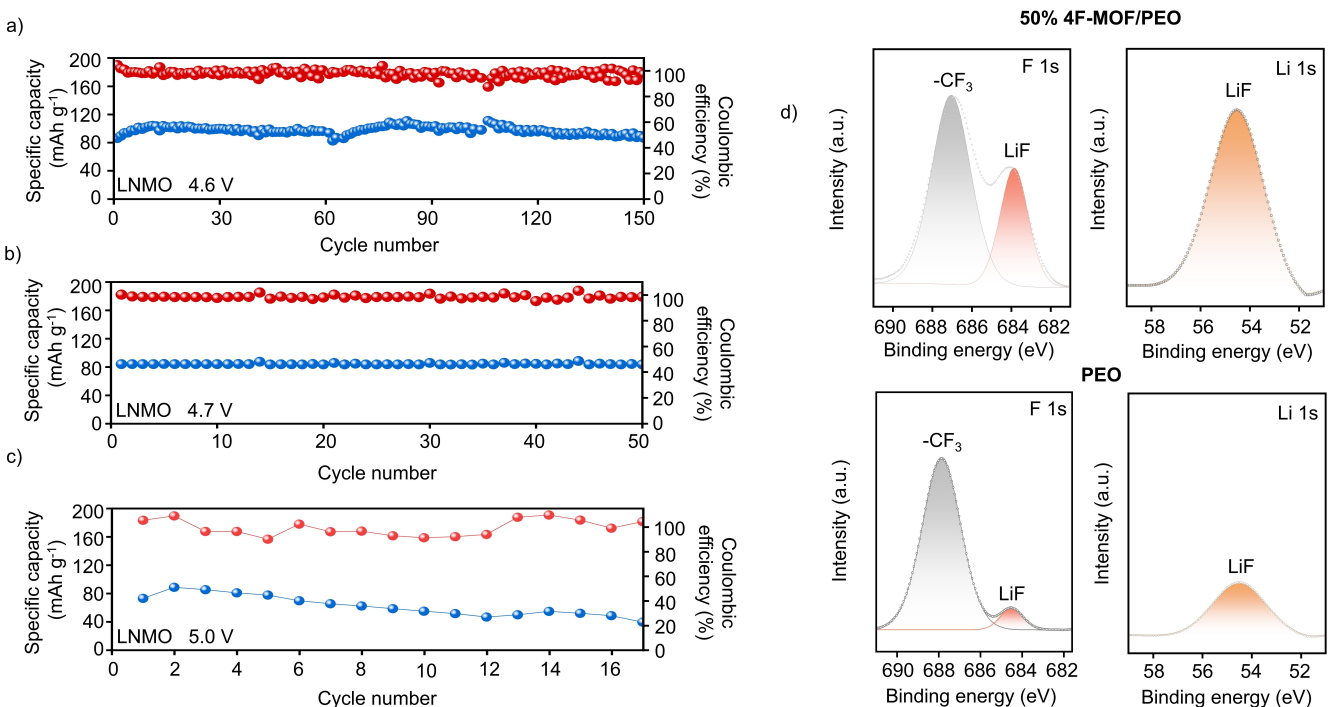


Figure 5. Charge-discharge cycling of 50 % 4F-MOF/PEO at high voltages. (a) Cycling performance in $\text{Li} \parallel \text{LNMO}$ cells at 0.1 C, 4.6 V and 60 °C. (b) Cycling performance in $\text{Li} \parallel \text{LNMO}$ cells at 0.1 C, 4.7 V and 60 °C. (c) Cycling performance in $\text{Li} \parallel \text{LNMO}$ cells at 0.1 C, 5.0 V and 60 °C. (d) XPS spectra of positive electrode surface after 150 cycles in cells containing 50.0 % 4F-MOF/PEO.

68.7 mAh·g⁻¹ to 42.8 mAh·g⁻¹ and could not function well, indicating the importance of fluorination.

To gain insights into the impact of 4F-MOF on the formation of the cathode electrolyte interphase (CEI) layer, we conducted an investigation on the interfacial layer of the positive electrodes (LNMO) via X-ray photoelectron spectroscopy (XPS). The cells underwent cycling with a 50 % 4F-MOF/PEO electrolyte at 5.0 V for 300 h. Analysis on C 1s and F 1s spectra was shown in Figure 5d. The two distinct peaks at 684.3 eV and 687.5 eV corresponded to LiF and CF₃, respectively. Notably, when compared to pure PEO electrolyte, the 50 % 4F-MOF/PEO electrolyte exhibited a higher LiF content within the CEI layer. The benefits of LiF on battery performance have been demonstrated, which can form a more compact and stable interface between the electrolyte and the electrode, thus protecting the electrolyte against oxidation.^[31] LiF could originate from the decomposition of LiTFSI, as well as the decomposition of 4F-MOF where the fluorine bonds break,^[32] which was subsequently deposited on the positive electrode's surface and effectively prevent electrolyte from oxidation in the subsequent cycles.

Conclusions

In conclusion, we obtained a fluorinated metal–organic framework (4F-MOF) with facileness, and utilized it as a composite electrolyte in lithium batteries. The as-prepared 50 % 4F-MOF/PEO solid-state electrolyte exhibited oxidative stability up to 5.0 V, and demonstrated no sign of lithium electrodeposition

instability of hundreds of charge-discharge cycles and over 1,300 operating hours in $\text{Li} \parallel \text{Li}$ symmetric cells. Due to the fluorine effect, a thin and uniform Li deposition layer and a LiF-rich CEI at the surface cathode was found, resulting in remarkable battery cycling performance up to 5.0 V. On basis of a variety of simulation and experimental investigations, we have shown that fluorination in MOF structures could not only lower the energy level of HOMO orbital due to the electron-withdrawing properties of F atoms and enhance the oxidative stability of solid-state electrolytes,^[33] but also form LiF-rich interfaces to suppress dendritic lithium proliferation^[34] and improve the electrolyte's stability at high cut-off voltages,^[35] expanding the capability of MOF-based solid-state electrolytes to work with high-voltage cathodes and metallic lithium anode simultaneously. Together with the good thermal, chemical, electrochemical stability as well as enhanced ion transport benefitted from fluorination, this novel fluorinated MOF-based material provides a promising approach for developing all-solid-state battery with high voltage tolerance and interfacial stability.

Supporting Information

Electrochemical testing and other supplementary material are available in Supporting Materials.

Acknowledgements

This work is financially supported by National Natural Science Foundation of China (22065037), Yunnan Fundamental Research Projects (202201AW070015, 202301AT070205) and Duke Kunshan University.

Conflict of Interests

The authors declare no competing financial interest.

Data Availability Statement

The data that support the findings of this study are available from the corresponding author upon reasonable request.

Keywords: Fluorinated electrolytes • Metal organic frameworks • Composite polymer electrolytes • All solid-state batteries • Solid-state electrolytes

- [1] M. Armand, J.-M. Tarascon, *Nature* **2008**, *451*, 652–657.
- [2] D. Lin, Y. Liu, Y. Cui, *Nat. Nanotechnol.* **2017**, *12*, 194–206.
- [3] Y. S. Meng, V. Srinivasan, K. Xu, *Science* **2022**, *378*, eabq3750.
- [4] W. Xu, J. Wang, F. Ding, X. Chen, E. Nasybulin, Y. Zhang, J.-G. Zhang, *Energy Environ. Sci.* **2014**, *7*, 513–537.
- [5] K. Xu, *Chem. Rev.* **2004**, *104*, 4303–4418.
- [6] J. B. Goodenough, Y. Kim, *Chem. Mater.* **2009**, *22*, 587–603.
- [7] R. Chen, Q. Li, X. Yu, L. Chen, H. Li, *Chem. Rev.* **2019**, *120*, 6820–6877.
- [8] Q. Zhao, S. Stalin, C.-Z. Zhao, L. A. Archer, *Nat. Rev. Mater.* **2020**, *5*, 229–252.
- [9] S. Xia, X. Wu, Z. Zhang, Y. Cui, W. Liu, *Chem* **2019**, *5*, 753–785.
- [10] X. Lin, M. Salari, L. M. R. Arava, P. M. Ajayan, M. W. Grinstaff, *Chem. Soc. Rev.* **2016**, *45*, 5848–5887.
- [11] Z. Li, H. Zhang, X. Sun, Y. Yang, *ACS Energy Lett.* **2020**, *5*, 3244–3253.
- [12] W. Zhou, Z. Wang, Y. Pu, Y. Li, S. Xin, X. Li, J. Chen, J. B. Goodenough, *Adv. Mater.* **2018**, *31*, e1805574.
- [13] J. Zhou, B. Wang, *Chem. Soc. Rev.* **2017**, *46*, 6927–6945.
- [14] T. Qiu, Z. Liang, W. Guo, H. Tabassum, S. Gao, R. Zou, *ACS Energy Lett.* **2020**, *5*, 520–532.
- [15] W. Li, W. Xie, F. Shao, J. Qian, S. Han, P. Wen, J. Lin, M. Chen, X. Lin, *Chem* **2023**, *9*, 117–129.
- [16] R. Zhao, Y. Wu, Z. Liang, L. Gao, W. Xia, Y. Zhao, R. Zou, *Energy Environ. Sci.* **2020**, *13*, 2386–2403.
- [17] A. J. Howarth, Y. Liu, P. Li, Z. Li, T. C. Wang, J. T. Hupp, O. K. Farha, *Nat. Rev. Mater.* **2016**, *1*, 15018.
- [18] X. Xu, G. Zhang, Y. Li, Q. Peng, *Chin. Chem. Lett.* **2019**, *30*, 809–825.
- [19] Z. Yu, H. Wang, X. Kong, W. Huang, Y. Tsao, D. G. Mackanic, K. Wang, X. Wang, W. Huang, S. Choudhury, Y. Zheng, C. V. Amanchukwu, S. T. Hung, Y. Ma, E. G. Lomeli, J. Qin, Y. Cui, Z. Bao, *Nat. Energy* **2020**, *5*, 526–533.
- [20] M. Jia, P. Wen, Z. Wang, Y. Zhao, Y. Liu, J. Lin, M. Chen, X. Lin, *Adv. Funct. Mater.* **2021**, *31*, 2101736.
- [21] S. Han, B. Wu, H. Wang, P. Wen, L. Zhang, X. Lin, M. Chen, *Angew. Chem. Int. Ed.* **2023**, *62*, e202308724.
- [22] H. Sun, X. Xie, Q. Huang, Z. Wang, K. Chen, X. Li, J. Gao, Y. Li, H. Li, J. Qiu, W. Zhou, *Angew. Chem. Int. Ed.* **2021**, *133*, 18483–18491.
- [23] Q. Zheng, Y. Yamada, R. Shang, S. Ko, Y.-Y. Lee, K. Kim, E. Nakamura, A. Yamada, *Nat. Energy* **2020**, *5*, 291–298.
- [24] M. Ma, F. Shao, P. Wen, K. Chen, J. Li, Y. Zhou, Y. Liu, M. Jia, M. Chen, X. Lin, *ACS Energy Lett.* **2021**, *6*, 4255–4264.
- [25] C. V. Amanchukwu, Z. Yu, X. Kong, J. Qin, Y. Cui, Z. Bao, *J. Am. Chem. Soc.* **2020**, *142*, 7393–7403.
- [26] X. Qing, J. Li, Z. Wang, M. Chen, J. Lin, X. Lin, *Chem. Commun.* **2020**, *56*, 15533–15536.
- [27] A. Kraytsberg, Y. Ein-Eli, *Adv. Energy Mater.* **2012**, *2*, 922–939.
- [28] J. H. Cavka, S. Jakobsen, U. Olsbye, N. Guillou, C. Lamberti, S. Bordiga, K. P. Lillerud, *J. Am. Chem. Soc.* **2008**, *130*, 13850–13851.
- [29] Z. Hu, Y. Peng, Z. Kang, Y. Qian, D. Zhao, *Inorg. Chem.* **2015**, *54*, 4862–4868.
- [30] Z. Li, L. Sun, L. Zhai, K.-S. Oh, J.-M. Seo, C. Li, D. Han, J.-B. Baek, S.-Y. Lee, *Angew. Chem. Int. Ed.* **2023**, *62*, e202307459.
- [31] X. Cao, P. Gao, X. Ren, L. Zou, M. H. Engelhard, B. E. Matthews, J. Hu, C. Niu, D. Liu, B. W. Arey, C. Wang, J. Xiao, J. Liu, W. Xu, J.-G. Zhang, *Proc. Natl. Acad. Sci. USA* **2021**, *118*, e2020357118.
- [32] Q. Liu, W. Jiang, J. Xu, Y. Xu, Z. Yang, D.-J. Yoo, K. Z. Pupek, C. Wang, C. Liu, K. Xu, Z. Zhang, *Nat. Commun.* **2023**, *14*, 3678.
- [33] Y. Wang, Z. Wu, F. M. Azad, Y. Zhu, L. Wang, C. J. Hawker, A. K. Whittaker, M. Forsyth, C. Zhang, *Nat. Rev. Mater.* **2024**, *9*, 119–133.
- [34] W. Zhang, V. Koverga, S. Liu, J. Zhou, J. Wang, P. Bai, S. Tan, N. K. Dandu, Z. Wang, F. Chen, J. Xia, H. Wan, X. Zhang, H. Yang, B. L. Lucht, A.-M. Li, X.-Q. Yang, E. Hu, S. R. Raghavan, A. T. Ngo, C. Wang, *Nat. Energy* **2024**, *9*, 386–400.
- [35] Y. Wang, Z. Wu, F. M. Azad, Y. Zhu, L. Wang, C. J. Hawker, A. K. Whittaker, M. Forsyth, C. Zhang, *Nat. Rev. Mater.* **2023**, *9*, 119–133.

Manuscript received: February 2, 2024

Revised manuscript received: March 30, 2024

Accepted manuscript online: April 12, 2024

Version of record online: May 8, 2024